Nuclear Science and Techniques (2026) 37:104
https://doi.org/10.1007/s41365-026-01949-8

The study of polarization properties of laser Compton slant scattering gamma beam at SLEGS

Xiang-Fei Wang[1,2,3] · Kai-Jie Chen[4] · Hang-Hua Xu[2,3] · Gong-Tao Fan[1,2,3] · Zi-Rui Hao[2] · Zhen-Wei Wang[1,3] · Long-Xiang Liu[2] · Yue Zhang[2] · Sheng Jin[1,3] · Qian-kun Sun[1,3] · Zhi-Cai Li[2,5] · Pu Jiao[2,6] · Meng-Die Zhou[2,6] · Yu-Long Shen[2,5] · Meng-Ke Xu[1,3] · Hong-Wei Wang[1,2,3]

Received: 28 September 2025 / Revised: 17 December 2025 / Accepted: 26 December 2025 / Published online: 26 March 2026

Abstract
Polarized high-energy photon gamma rays are excellent probes for nuclear and particle physics research. Recently, a unique method for generating MeV energy-tunable gamma rays, the Laser Compton Slant Scattering (LCSS) mode, was implemented at the Shanghai Laser Electron Gamma Source (SLEGS). A study of the polarization properties of the LCSS gamma beam at SLEGS combined theoretical simulations with experimental measurements. The intensity of spatial distributions and Stokes parameters were systematically simulated for LCSS of linearly/circularly polarized laser photons and unpolarized relativistic electrons. The measured scattered gamma spatial distributions at three typical slant incidence angles were in agreement with the simulation for the linearly polarized laser. The results imply that the polarization degree of the incident photon is almost completely transferred to the scattered gamma rays for any incident angle, while the direction of polarization of the scattered gamma ray changes with the incident and scattering angles.

Keywords Laser Compton slant scattering · SLEGS · Polarized gamma beam · Stokes parameter

1 Introduction

Gamma rays, which are high-energy photons, possess the inherent advantage of relative insensitivity to strong nuclear forces during nuclear reactions. This characteristic enables a variety of high-precision experiments, such as polarization measurements, studies of weak interaction processes, and investigations into fundamental physics issues such as isospin non-conservation [1, 2].

Polarization is a key characteristic of gamma photons, representing a fundamental quantum degree of freedom analogous to properties such as spin and isospin. For linearly polarized gamma beams, the polarization direction provides essential information by revealing the dependence of the differential scattering cross section on the relative azimuthal angle between the polarization vector and the production plane. The use of linearly polarized beams significantly simplifies the experimental design by providing an additional observable, enabling effective discrimination between competing transition mechanisms. Circularly polarized gamma photons possess a definite helicity ($\pm$ 1), corresponding to the projection of the photon's

This work was supported by the National Key R&D Program (Nos. 2023YFA1606901, 2022YFA1602400), the National Natural Science Foundation of China (Nos. 12275338, 12388102, U2441221), and Shanghai Oriental Talents-Leading Project (No. LJ2024080).

✉ Hang-Hua Xu
xuhh@sari.ac.cn

✉ Gong-Tao Fan
fangt@sari.ac.cn

1 Shanghai Institute of Applied Physics, Chinese Academy of Sciences, Shanghai 201800, China

2 Shanghai Advanced Research Institute, Chinese Academy of Sciences, Shanghai 201210, China

3 University of Chinese Academy of Sciences, Beijing 101408, China

4 School of Physical Science and Technology, ShanghaiTech University, Shanghai 201210, China

5 School of Nuclear Science and Technology, University of South China, Hengyang 421001, China

6 School of Physics, Henan Normal University, Xinxiang 453007, China

spin angular momentum onto its momentum direction. This well-defined helicity provides unique experimental capabilities. When combined with longitudinally polarized target particles, the helicities of both the beam and target can be employed to prepare an initial state with a precisely defined total angular momentum projection. This control significantly enhances the precision and information content of the experimental measurements.

There are two main methods for generating polarized gamma beams using accelerators: bremsstrahlung and Laser Compton Scattering (LCS). In the 1950s and the 1960s, several polarized bremsstrahlung gamma beams with photon energies of 10–20 MeV were produced to study the giant electric-dipole resonance in nuclei [3, 4]. Higher-energy bremsstrahlung gamma beams of approximately 350 MeV were also developed to measure the cross sections for pion photoproduction in the 1960s [5]. The first linearly polarized gamma beams, with a polarization degree of the order of 30–50%, were produced by exploiting the natural polarization of bremsstrahlung when the photons were collimated at a small solid angle away from the direction of the primary electrons [6, 7]. The first polarized LCS gamma beam was achieved in 1987 at the Adone storage ring in Frascati with a laser-electron head on collision, known as the Laser Compton Back Scattering (LCBS) [8]. Gamma beams produced by the LCBS method offer nearly 100% Degree Of Polarization (DOP), combined with advantages such as a small divergence angle, narrow energy bandwidth, and high spectral brightness. Following the early successes at Adone, several polarized gamma beam facilities using this method have been established at several other storage rings, such as ROKK-1 M at the Novosibirsk Laboratory in Russia [9], GRAAL at ESRF in France [10], and LEGS at NSRF

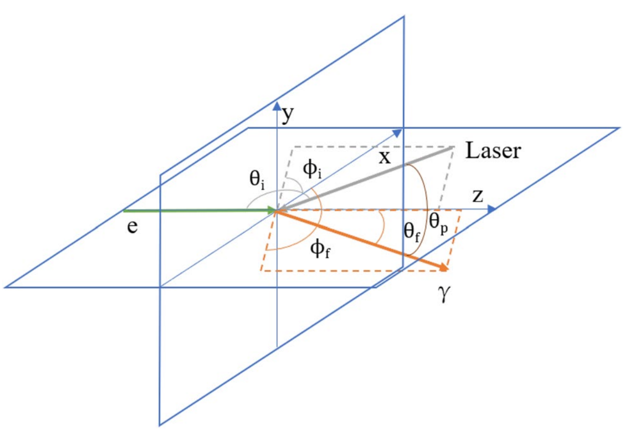

Fig. 1 The scattering process of relativistic electrons and laser photons in the laboratory system. θ_i and ϕ_i are the azimuthal angles of the incident laser photon, θ_f and ϕ_f are the azimuthal angles of the scattered photon, θ_p is the angle between the incident laser beam stream and the outgoing gamma beam stream

in the United States [11]. Several gamma LCBS-polarized gamma beams are currently in operation for users. HIγS in the United States can produce 1–100 MeV polarized gamma beams, allowing it to carry out a set of high-precision Nuclear Resonance Fluorescence(NRF) experiments [12]. Meanwhile, GeV-polarized gamma beams are produced at LEPS and LEPS2 at SPring-8 in Japan, contributing to the understanding of nucleon resonance [13, 14].

The Laser Compton Slant Scattering (LCSS) technique offers an alternative method for generating polarized gamma rays. Unlike head-on collisions, LCSS produces photons via Compton scattering between a laser and an electron beam at a collision angle smaller than 180° relative to the electron beam direction. The corresponding incident angles are referred to as slanting incident angles in this paper. The feasibility of the LCSS was first demonstrated in 1996 [15]. More recently, MeV-range polarized gamma beams with high polarization purity and brilliance have been successfully produced via LCSS at 90° incident angles at the UVSOR-III electron storage ring [16–19].

The polarization properties of LCS gamma rays have been theoretically discussed by several research groups. A theoretical analysis of LCBS-polarized gamma-ray properties was performed in HIγS [20], where the integral values of polarization-related variables were provided by an MCCMPT simulation code within the QED framework. Reference [21] has analyzed the polarization of LCBS X/gamma rays produced in SPARC-LAB device and ELI-NP facility in both classical and quantum schemes. The classical electrodynamics treatment of the photon polarization transfer during the LCSS process in the X-ray Thomson energy region is given in Refs. [22–27]. In UVSOR-III, the polarization properties of LCSS MeV gamma rays generated between a 750 MeV electron beam and an 800 nm polarized laser at a certain slant incident angle of 90° were calculated using the Lienard–Wiechert potentials [17, 18].

The Shanghai Laser Electron Gamma Source (SLEGS) is a new MeV LCSS gamma-ray facility. By adjusting the slant incident angle, in a range from 20° to 160°, between the polarized 10.64 μm CO_2 laser and the 3.5 GeV electron beams in the storage ring of the Shanghai Synchrotron Radiation Facility (SSRF) [28, 29], SLEGS produces polarized gamma rays ranging from 0.66 to 21.1 MeV [30–38]. In contrast to the UVSOR-III gamma rays produced via LCSS at a 90° incident angle, SLEGS is a new class of tunable gamma rays generated using the LCSS process over a wide range of continuously tunable incident angles. The polarization of gamma rays is one of the properties that SLEGS users are most concerned with.

To analyze the polarization properties of the LCSS gamma rays in SLEGS and provide a more explicit representation of the LCSS process, we developed a simulation code based on the QED framework. Using the simulation codes, the polarization properties of the LCSS gamma beam generated by SLEGS, including the spatial and polarization distributions

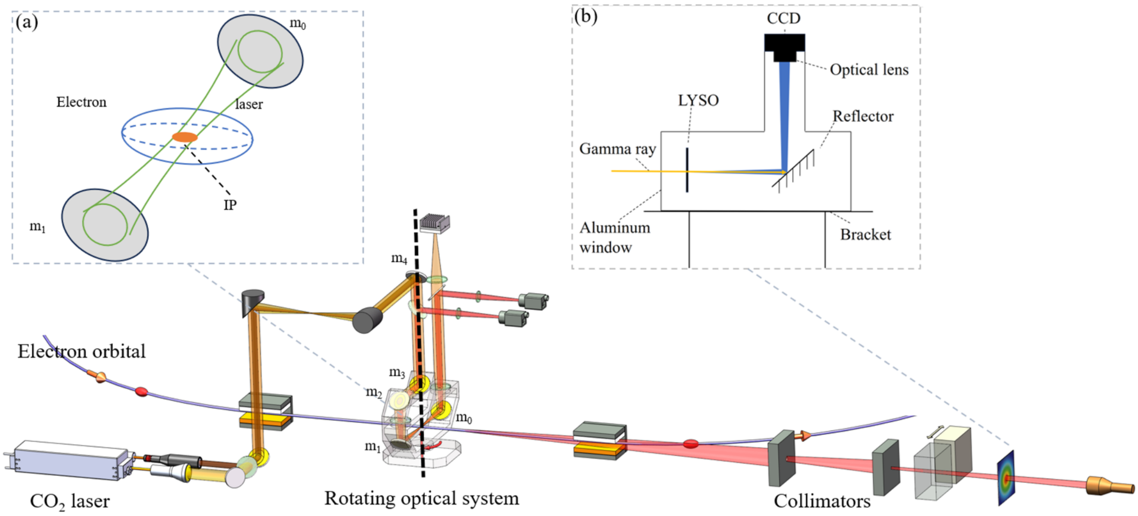

Fig. 2 (Color online) Schematic diagram of the SLEGS LCSS mode. **a** Intersection of laser with electron bunch, b Configuration of GSM. The gamma beam enters the dark box through the front aluminum window and hits the LYSO crystal of Φ76 × 2 mm vertically. The camera was mounted at the top of the dark box, perpendicular to the beam direction. To acquire fluorescence from the LYSO crystal, a mirror was inserted into the beam path back to the target at 45° with respect to the beam direction. The inner surface of the dark box has been anodized to prevent fluorescent reflection

with linearly/circularly polarized lasers, were obtained over a wide range of incident angles. To confirm the reliability of the simulation, the spatial distributions of LCSS gamma rays with a linearly polarized CO_2 laser were measured and compared with the simulation results.

The remainder of this paper is organized as follows: Sect. 2 presents the theoretical framework for the LCSS process. Section 3 introduces the LCSS setup used in this study. Section 4 presents the simulation results. Section 5 provides a comparative analysis of the simulated and measured results of the proposed model. Finally, Sect. 6 provides a summary of the study.

2 Polarization theory of LCSS mode

2.1 Differential scattering cross sections and gamma-ray distribution

The geometry of the LCSS process at the interaction point (IP) in the laboratory frame is illustrated in Fig. 1. The incident electron with momentum **p** moves along the z-direction. The incident laser photon with momentum **k** propagates along the direction defined by the angles θ_i and ϕ_i. After slant scattering, the scattered photon possesses a momentum $\mathbf{k}'$ directed along the angles θ_{f} and ϕ_{f}.

According to classical electrodynamics and quantum electrodynamics (QED) [39], the scattering process of electrons and photons can be given by

Table 1 Electron beam parameters at the SLEGS interaction point (IP)

Parameter	Value
Electron kinetic energy, E_e (GeV)	3.5
Repetition rate, f (MHz)	347
Bunch charge, eN_e (pC)	576
Transverse normalized rms emittance, ϵ_N (mm mrad)	4.21
rms bunch length, $\Delta\tau$ (mm)	53
Relative energy spread	1.11×10^{-3}
The electron beam momentum spread, ϵ_x (nm rad)	4.1270
Twiss parameter, α_x	0.3085
Twiss parameter, β_x (m)	9.11
Twiss parameter, γ_x (m^{-1})	0.1200
Electron bunch spot size, σ_x (μm)	311.6
The electron beam momentum spread, ϵ_y (nm rad)	0.0253
Twiss parameter, α_y	−0.1199
Twiss parameter, β_y (m)	4.13
Twiss parameter, γ_y (m^{-1})	0.2454
Electron bunch spot size, σ_y (μm)	10.23
Dispersion function, η_x (m)	0.2176

$$\mathbf{p} + \mathbf{k} = \mathbf{p}' + \mathbf{k}', \quad (1)$$

where **p** and **k** are the four-momenta of the incident electron and photon, respectively, and $\mathbf{p}'$ and $\mathbf{k}'$ are the four-momenta of the scattered electron and photon, respectively. Considering the conservation of momentum and some simple

Table 2 Laser parameters at the SLEGS interaction point (IP)

Parameter	Value
Wavelength, λ_{laser} (nm)	10,640
Photon energy, E_{laser} (eV)	0.117
Laser power (W)	< 137
Linear polarization	100%
Spot size, σ_{laser} (μm)	70
Directional stability (μrad)	<4
Interaction angle (°)	20–160
Rotation step size (°)	0.0002

transformations, the energy of the scattered photon E_g can be written as

$$E_g = \frac{(1-\beta\cos\theta_i)E_p}{(1-\beta\cos\theta_f)+(1-\beta\cos\theta_p)\frac{E_p}{E_e}}, \tag{2}$$

where E_p and E_e are the energies of the incident laser photon and electron, respectively. The relationship between these angles is illustrated in Fig. 1. And θ_p is calculated by the formula

$$\cos\theta_p = \cos\theta_i\cos\theta_f + \sin\theta_i\sin\theta_f\cos(\phi_i-\phi_f). \tag{3}$$

According to the conclusion in QED, the differential cross section of unpolarized electrons scattering with linearly polarized photons is given as [40]

$$\frac{d\sigma}{d\Omega} = \frac{8r_e^2}{X^2}\left\{[1+P_t\cos(2\tau-2\phi_f)]\left[\left(\frac{1}{X}-\frac{1}{Y}\right)^2+\frac{1}{X}-\frac{1}{Y}\right] + \frac{1}{4}\left(\frac{X}{Y}+\frac{Y}{X}\right)\right\}\left(\frac{E_g}{mc^2}\right)^2, \tag{4}$$

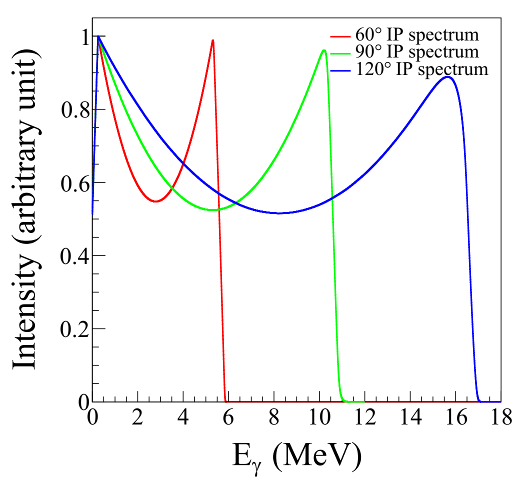

Fig. 3 (Color online) Simulated gamma-ray energy distributions produced in LCSS mode at the slant incident angles, θ_i, 60°, 90° and 120° (normalized)

where r_e represents the classical electron radius, P_t is the degree of linear polarization of the incident laser, τ is the rotation angle of the polarization direction, and mc^2 is the electron rest mass energy. X and Y are Lorentz invariants, calculated by the formula

$$X = \frac{s-(mc)^2}{(mc)^2}, Y = \frac{(mc)^2-u}{(mc)^2}, \tag{5}$$

where s and u are Mandelstam variables calculated by the formula [39]

$$s = (\mathbf{p}+\mathbf{k})^2, u = (\mathbf{p}-\mathbf{k}')^2. \tag{6}$$

Considering that the phase space of the electron pulse and the intensity distribution of the laser beam have an effect on the distribution of gamma-ray beam, the calculation formulas are introduced as follows

$$f_e(x,y,z,x',y',p,t) = \frac{1}{(2\pi)^3\epsilon_x\epsilon_y\sigma_p\sigma_z} \exp\left[-\frac{\gamma_x x^2+2\alpha_x xx'+\beta_x x'^2}{2\epsilon_x} - \frac{\gamma_y y^2+2\alpha_y yy'+\beta_y y'^2}{2\epsilon_y} - \frac{(p-p_0)^2}{2\sigma_p^2} - \frac{(z-z_0)^2}{2\sigma_z^2}\right], \tag{7}$$

$$f_p(x_l,y_l,z_l,k,t) = \frac{1}{4\pi^2\sigma_k\sigma_l\sigma_w^2} \exp\left[-\frac{x_l^2+y_l^2}{2\sigma_w^2} - \frac{(z_l+ct)^2}{2\sigma_l^2} - \frac{(k-k_0)^2}{2\sigma_k^2}\right], \tag{8}$$

where the formula for σ_w is

$$\sigma_w = \sqrt{\frac{\lambda\beta_0}{4\pi}\left(1+\frac{z_1^2}{\beta_0^2}\right)}. \tag{9}$$

Here, c is the speed of light, p is the electron momentum, p_0 is the electron center momentum, x' and y' are the

Table 3 Simulation result of spatial distribution with a linearly polarized laser in LCBS

Laser polarization direction	Arbitrary	Horizontal	Vertical
Electron phase space distribution	Unconsidered	Considered	Considered
FWHM along short axis (mm)	4.0	4.3	4.0
FWHM along long axis (mm)	7.6	7.8	7.8

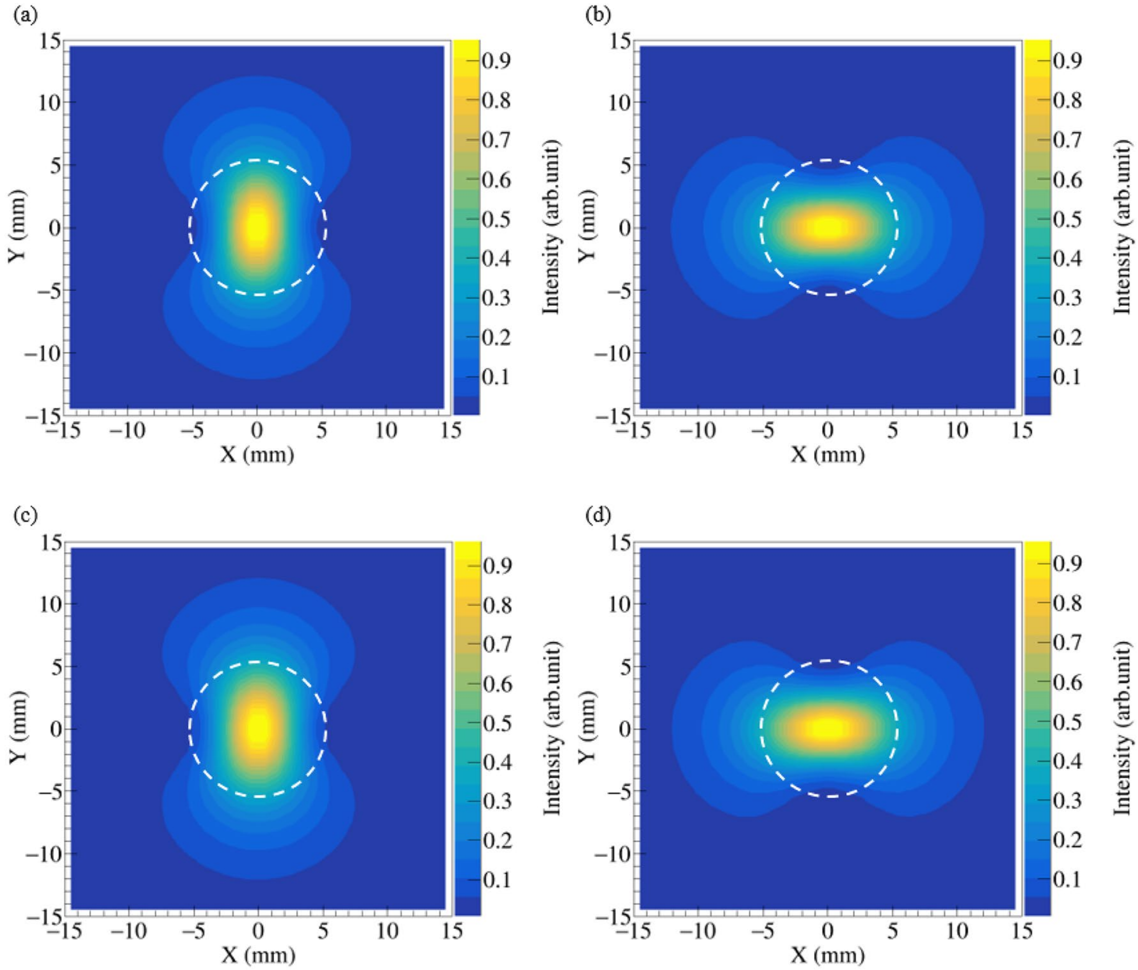

Fig. 4 (Color online) Simulation of fully linearly polarized gamma-ray beam spatial distribution. **a**, **c** are horizontally polarized gamma-ray beam spots, **b**, **d** are vertically polarized gamma-ray beam spots. **a**, **b** show the simulation results without considering the phase space of the electron pulse and the intensity distribution of the laser, while **c** and **d** show the simulation results considering the phase space of the electron pulse and the intensity distribution of the laser. The white dashed circle represents the position of the beam spot corresponding to when the scattering angle reaches $1/\gamma$, where γ is the Lorentz factor of the electron beam. The intensities shown in the figures are all relative intensities normalized to 1

angular divergence of the electron in the x and y-direction, $\alpha_{x,y}, \beta_{x,y}, \gamma_{x,y}$ are the Twiss parameters of the electron, and $\epsilon_{x,y}, \sigma_{p,z}$ are the momentum spread of the electron beam; and k is the wavevector of the laser photon, k_0 is the center wavevector of the laser photon, and $\beta_0, \sigma_p, \sigma_1$ are the Rayleigh range, energy diffusion, and beam length of the laser beam, respectively.

2.2 Stokes parametric simulation

Considering the polarized nature of the incident photon and scattered photon, the differential scattering cross section of the scattered photon can be written as [20]

$$\begin{aligned}\frac{d\sigma}{dYd\phi_f} =& \frac{2r_e^2}{X^2}\left\{\left(\frac{1}{X}-\frac{1}{Y}\right)^2+\frac{1}{X}-\frac{1}{Y}+\frac{1}{4}\left(\frac{X}{Y}+\frac{Y}{X}\right)\right.\\ &-(\xi_3+\xi_3')\left[\left(\frac{1}{X}-\frac{1}{Y}\right)^2+\frac{1}{X}-\frac{1}{Y}\right]\\ &+\xi_1\xi_1'\left(\frac{1}{X}-\frac{1}{Y}+\frac{1}{2}\right)\\ &+\xi_2\xi_2'\frac{1}{4}\left(\frac{X}{Y}+\frac{Y}{X}\right)\left(1+\frac{2}{X}-\frac{2}{Y}\right)\\ &\left.+\xi_3\xi_3'\left[\left(\frac{1}{X}-\frac{1}{Y}\right)^2+\frac{1}{X}-\frac{1}{Y}+\frac{1}{2}\right]\right\}.\end{aligned} \tag{10}$$

After simplification, the formula for the differential scattering cross section is obtained as follows:

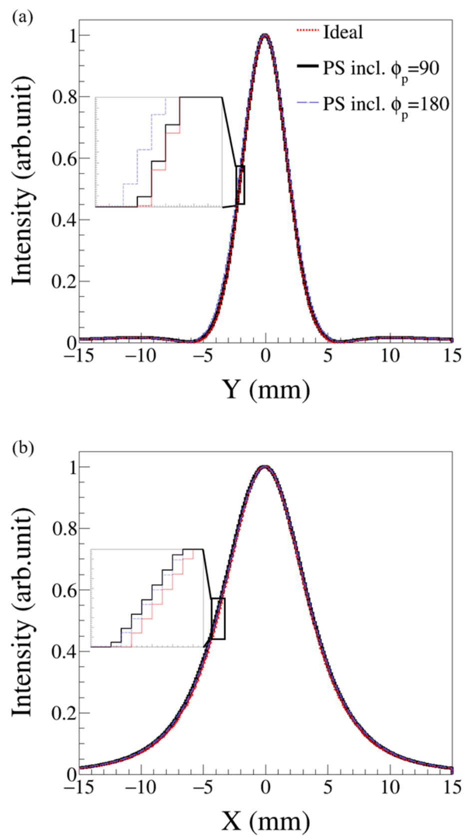

Fig. 5 (Color online) Simulation of intensity profiles of cross sections taken along the short and long axes passing through the gamma-ray spot center. The fully ideal case (cyan line) and the cases with laser polarization directions of 90° (red line) and 180° (purple line) after adding the electron position and momentum information. Where **a** is the slice at the short axis of the calculated spot and **b** is the slice at the long axis of the calculated spot

$$\xi_1 = P_\mathrm{t}\sin(2\tau - 2\phi_\mathrm{f}), \xi_2 = P_\mathrm{c}, \xi_3 = -P_\mathrm{t}\cos(2\tau - 2\phi_\mathrm{f}), \tag{11}$$

$$\frac{\mathrm{d}\sigma}{\mathrm{d}Y\mathrm{d}\phi_\mathrm{f}} = \frac{2r_\mathrm{e}^2}{X^2}\left(\Phi_0 + \sum_{i=1}^{3}\Phi_i\xi_i^\mathrm{f}\right), \tag{12}$$

$$\begin{aligned}\Phi_0 =&\left(\frac{1}{X}-\frac{1}{Y}\right)^2 + \frac{1}{X} - \frac{1}{Y}\\ &+ \frac{1}{4}\left(\frac{X}{Y}+\frac{Y}{X}\right)\\ &- \left[\left(\frac{1}{X}-\frac{1}{Y}\right)^2 + \left(\frac{1}{X}-\frac{1}{Y}\right)\right]\xi_3,\end{aligned} \tag{13}$$

$$\begin{aligned}\Phi_1 =& -\left(\frac{1}{X}-\frac{1}{Y}\right.\\ &\left.+\frac{1}{2}\right)\xi_1\cos 2\phi_\mathrm{f} - \left\{\left[\left(\frac{1}{X}-\frac{1}{Y}\right)^2\right.\right.\\ &\left.+\frac{1}{X}-\frac{1}{Y}+\frac{1}{2}\right]\xi_3\\ &-\left[\left(\frac{1}{X}-\frac{1}{Y}\right)^2\right.\\ &\left.\left.+\left(\frac{1}{X}-\frac{1}{Y}\right)\right]\right\}\sin 2\phi_\mathrm{f},\end{aligned} \tag{14}$$

$$\Phi_2 = \frac{1}{4}\left(\frac{X}{Y}+\frac{Y}{X}\right)\left(\frac{2}{X}-\frac{2}{Y}+1\right)\xi_2, \tag{15}$$

$$\begin{aligned}\Phi_3 =&\left(\frac{1}{X}-\frac{1}{Y}+\frac{1}{2}\right)\xi_1\sin 2\phi_\mathrm{f}\\ &-\left\{\left[\left(\frac{1}{X}-\frac{1}{Y}\right)^2+\frac{1}{X}-\frac{1}{Y}+\frac{1}{2}\right]\xi_3\right.\\ &\left.-\left[\left(\frac{1}{X}-\frac{1}{Y}\right)^2+\left(\frac{1}{X}-\frac{1}{Y}\right)\right]\right\}\cos 2\phi_\mathrm{f},\end{aligned} \tag{16}$$

$$\xi_i^\mathrm{f} = \frac{\Phi_i}{\Phi_0}, i = 1, 2, 3 \tag{17}$$

where ξ_i and ξ_i^f are the Stokes parameters of the incident and scattered photons, respectively, and τ is the polarization rotation angle.

According to Fig. 1, the Stokes parameter ξ_1^f is defined as positive along the directions in the first and third quadrants of the $x-y$ plane along the line defined by $y = x$, and negative along the second and fourth quadrants, along the line defined by $y = -x$. The Stokes parameter ξ_2^f is defined as positive for left-handed circular polarization about the z-axis and negative for right-handed circular polarization. The Stokes parameter ξ_3^f is defined as positive along the x-axis and negative along the y-axis.

3 LCSS setup at SLEGS

The SLEGS was approved in 2016 as one of the 16 beamlines in the Phase II project of the SSRF [41, 42]. The beamline passed the commissioning test in 2021 and was opened to users at the end of 2022 [43]. A schematic representation of the SLEGS is shown in Fig. 2.

The CO_2 laser was 100% linearly polarized and operated in a gated CW mode with an output power range of 0.1–137 W. A 632.8 nm visible He-Ne laser was coaxial to act as a reference beam to align the invisible CO_2 laser. The laser beam then propagates through a laser transport system [44], including a set of plane mirrors and a pair of

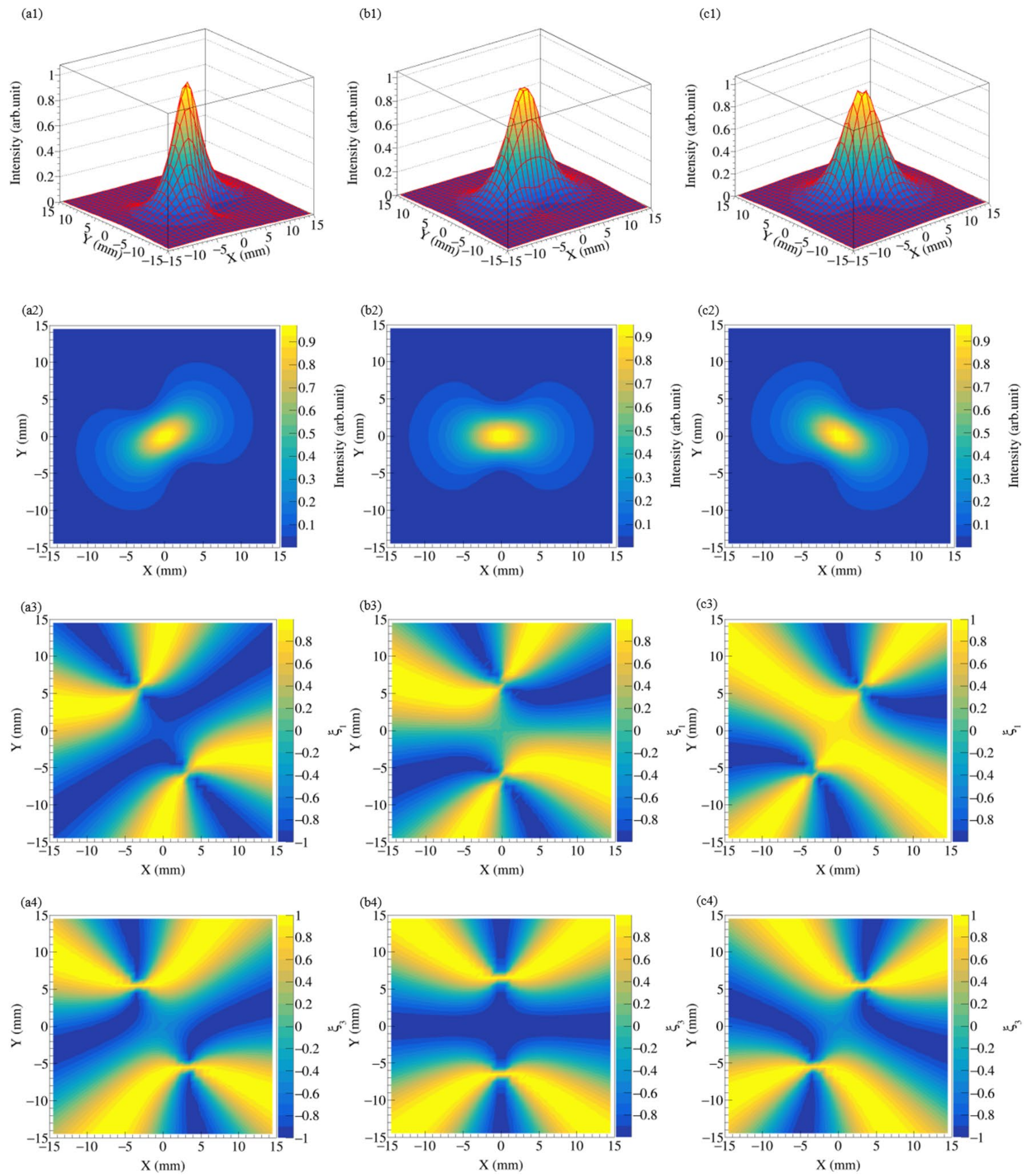

Fig. 6 (Color online) Simulations for LCSS of a Gaussian CO_2 10,640 nm laser beam with 100% linear polarization on realistic 3.5 GeV electron beam in three typical slant incident angles 60°, 90°, and 120°. **a1**, **b1**, **c1** three-dimensional intensity gamma beam distribution in the three typical slant incident angles; **a2**, **b2**, **c2** two-dimensional intensity gamma beam distribution in the three typical slant incident angles; **a3**, **b3**, **c3** the distributions of the Stokes covariates ξ_1^f; **a4**, **b4**, **c4** the distributions of the Stokes covariates ξ_3^f. All simulation results were calculated in the laboratory frame, and the imaginary position was placed 42 m downstream of the IP

off-axis parabolic mirrors, to the IP for the LCSS process. A position feedback system consisting of a CCD camera and piezoelectric ceramic driver system was installed at the end of the path. This effectively suppresses the drift and jitter of the laser pointing direction. The total length of the laser transportation path was approximately 25 m.

A rotatable optical system was installed at the center of the C03 section of the SSRF storage ring to introduce the laser into the IP [30]. A 3D structural diagram is shown in Fig. 2. The CO_2 laser beam is vertically injected along the rotation axis through m_4, guided through m_3, m_2 and m_1, and horizontally led to the IP to collide with the electron

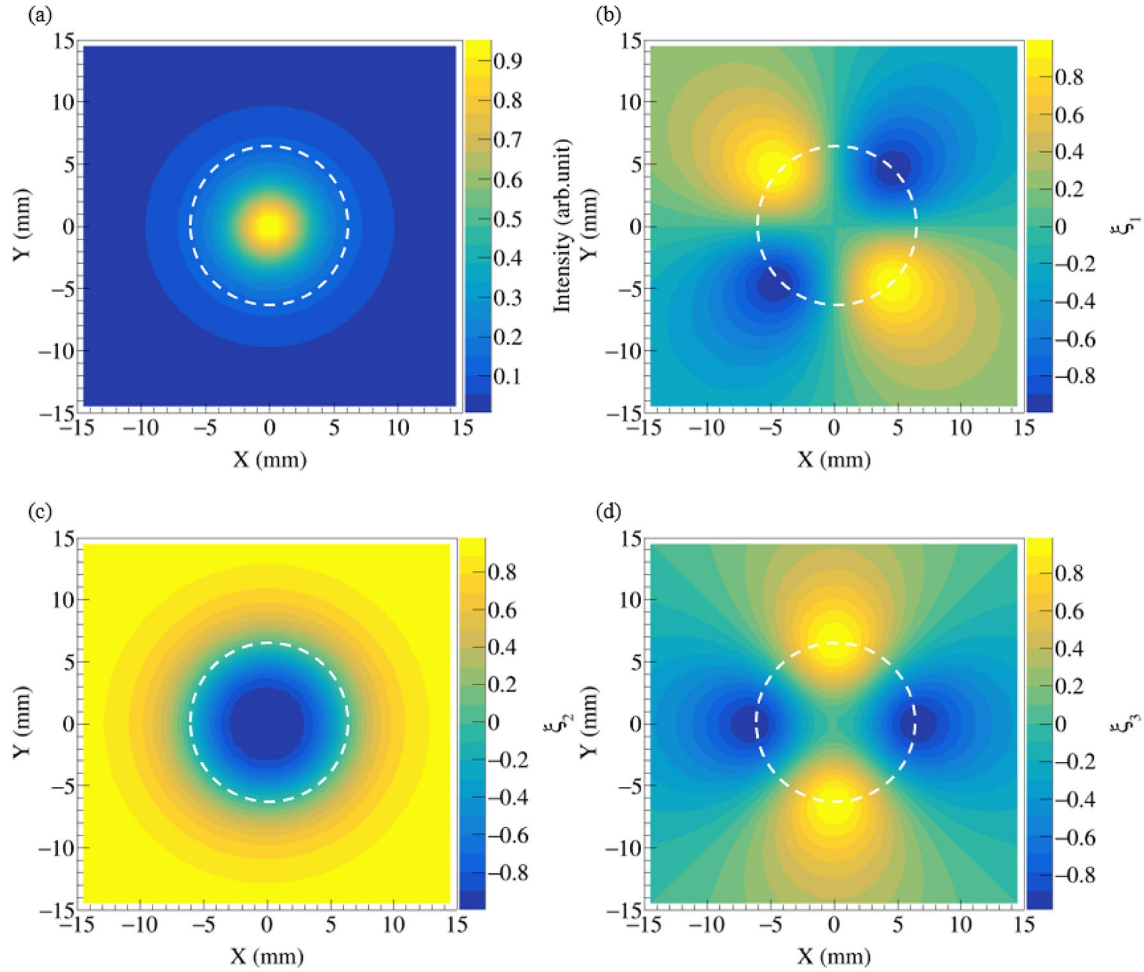

Fig. 7 Simulations for LCSS of a Gaussian CO_2 10,640 nm laser beam with 100% circular polarization on realistic 3.5 GeV electron beam in a typical slant incident angles 90°. **a** the relative intensity gamma beam distribution. **b–d** are the distributions of the Stokes covariates ξ_1^f, ξ_2^f, and ξ_3^f, respectively. All simulation results were calculated in the laboratory frame, and the imaginary position was placed 42 m downstream of the IP. The circle formed by the white dotted line is the $1/\gamma$ position, where γ is the Lorentz factor of the 3.5 GeV electron

beam in an angular range of 20°−160°. After passing through the IP, the laser beam was guided through m_0 to a water-cooled laser beam dump. The parameters of the CO_2 laser and electrons at the IP are listed in Tables 1 and 2.

It can be deduced through geometry that the rotation of the mirror group from the m_3 to the m_1 mirror along the axis leads to the rotation of the laser spot at the IP, which consequently results in the rotation of the polarization direction. The alteration in the direction of polarization was equivalent to the change in the slanting incident angle of the laser.

The gamma beam generated by the LCSS process travels approximately 42 m and passes through multiple collimators before arriving at the experimental station for imaging. A Gamma Spot Monitor (GSM) [45] was used to measure the gamma spot. It consists of a LYSO crystal to generate fluorescence, an optical transmission path, a camera to collect fluorescence, and a data acquisition system. The structure of the GSM is illustrated in Fig. 2 (b). The contrast resolution was better than 14%. The spatial resolution of the imaging system was characterized by the modulation transfer function (MTF), which was 6.4 lp/mm.

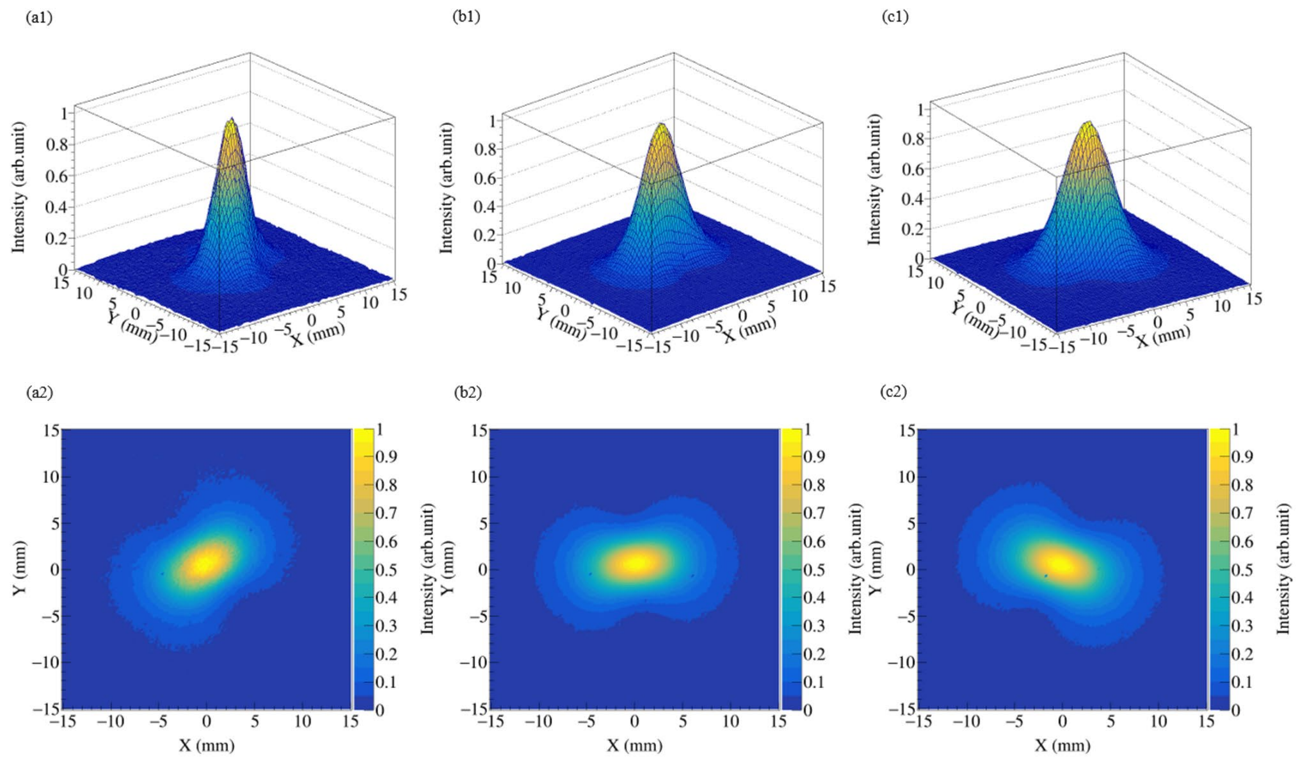

Fig. 8 (Color online) Measured GSM gamma-ray image for a 100% linearly polarized CO_2 10,640 nm laser beam slant scattered on realistic 3.5 GeV electron beam in three angles 60°, 90°, and 120°. **a1**, **b1**, **c1** Three-dimensional intensity gamma beam distribution at the three slant incident angles; **a2**, **b2**, **c2** Two-dimensional intensity gamma beam distribution at the three slant incident angles

4 Simulation results

4.1 Energy distribution

The LCSS energy distribution at IP simulated in three typical slant incident angles of 60°, 90°, and 120° is shown in Fig. 3. The results show that as the slant incident angle increases, the gamma-ray spectrum shifts regularly toward higher energies, illustrating the angular dependence of the gamma-ray energy in the LCSS mode.

4.2 Spatial and polarization distribution with linearly polarized laser

Here, we assume that the incident CO_2 laser is fully linearly polarized (100%), with its polarization azimuth oriented horizontally or vertically. It should be noted that in the LCSS process, the azimuthal angle is defined relative to the axis of the laboratory coordinate system.

First, the effects of the shapes of the electron beam and laser, as well as the momentum distribution of the electron beam on the spatial distribution of the LCSS gamma ray, were analyzed. By using Eqs. (7) and (8), calculations of the ideal condition versus the condition including the above-mentioned distribution in the phase space of electron and laser have been carried out in the 180° laser Compton back scattering process. Figure 4 shows the spatial distribution of the simulated gamma rays at the GSM position. The calculation was performed with a 100% linearly polarized incident laser with associated Stokes coefficients ξ_3 equal to 1 and −1, respectively. This shows that the spatial intensity distribution of linearly polarized gamma rays varies with the polarization angle and is azimuthally "symmetric". Figure 5 shows the intensity profiles of the cross sections taken along the short and long axes, passing through the center of the light spot. From Figs. 4 and 5, the diffusion due to the phase space distribution is not significant compared to the ideal condition. The specific numerical values are summarized in Table 3.

Considering that the electronic phase space and laser intensity distribution do not significantly affect the intensity distribution of the gamma spot, the ideal model was employed to simulate the spatial distribution of polarization. The spatial distribution and polarization distribution in three typical slant incident angles of 60°, 90°, and 120° on GSM are systematically simulated and shown in Fig. 6. The three incident angles are 60° (a1–a4), 90° (b1–b4), and 120° (c1–c4). For each angle, the subpanels correspond to the 3D surface plot of the gamma-ray intensity, its 2D

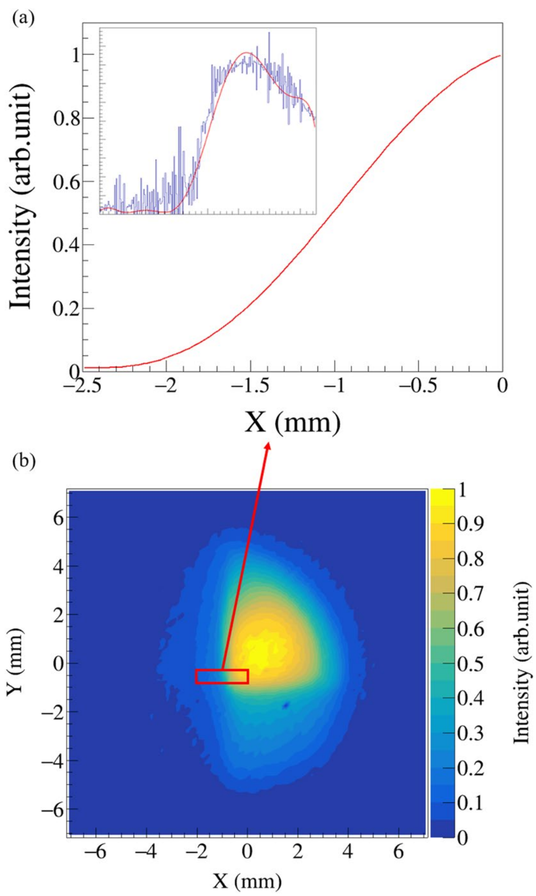

Fig. 9 **a** Polynomial-fitted curve for selected experimental data regions; **b** results from the knife edge measurement method

Table 4 Measured results of spatial distribution with a linearly polarized laser in LCSS

Parameter	Gamma spot size (mm)		
	60°	90°	120°
FWHM along short axis (mm)	4.6	4.6	4.6
FWHM along long axis (mm)	7.8	8.1	8.1

pseudocolor representation, and the distributions of the Stokes parameters $\xi_1^{\rm f}$ and $\xi_3^{\rm f}$.

The three-dimensional intensity distribution (Fig. 6a1, b1, c1) and intensity distribution (Fig. 6a2, b2, c2) show that the azimuthally asymmetric linearly polarized gamma-ray spots rotate with the slant incident angle. The distributions of the Stokes covariates $\xi_1^{\rm f}$ and $\xi_3^{\rm f}$ for different slant incident angles (Fig. 6a3, b3, c3) suggest that the gamma-ray's angle of linearly polarization changes with the slant incident angle. The DOP of scattered gamma ray is jointly determined by $\xi_1^{\rm f}$ and $\xi_3^{\rm f}$, the value is $\sqrt{(\xi_1^{\rm f})^2 + (\xi_1^{\rm f})^2}$ in the ideal condition. From the distributions of the Stokes covariates $\xi_1^{\rm f}$ and $\xi_3^{\rm f}$ (Fig. 6a3, a4, b3, b4, c3, c4), the present simulation shows that the DOP remains almost 1 within the scattering angle of $1/\gamma$, where γ is the Lorentz factor. This suggests that the DOP is completely transferred from the incident CO_2 laser photon to the scattered gamma ray and does not show significant changes with different slant incident angles. This result is also consistent with the prediction of Filipescu's simulation in Ref. [46]. If this conclusion is confirmed experimentally, it implies that highly polarized gamma rays can be produced based on the LCSS process using an incident laser with a high DOP at any slant incident angle.

4.3 Spatial and polarization distribution with circularly polarized laser

To compare with the linearly polarized scenario, a fully circularly polarized CO_2 laser was used in the analysis. Because the SLEGS LCSS process changes the direction of the incident laser polarization in a manner similar to the effect of a 1/2 wave plate, the polarization direction of the scattered gamma rays from the LCSS would not change if a circularly polarized laser was injected at different slant incident angles. The spatial distribution and polarization distribution in a typical slant incident angles of 90° on GSM are simulated and shown in Fig. 7.

The simulation results indicate that the circularly polarized photons undergo a flip in their helicity following slant Compton scattering with unpolarized electrons, for instance, changing from a left-handed circularly polarized laser to a right-handed circularly polarized gamma ray. In the case of a linearly polarized laser, which can be viewed as a superposition of left- and right-handed circularly polarized components, this phenomenon remains concealed.

It is worth noting that as the radius of the beam spot increases, the DOP of circular polarization gradually decreases to 0, takes on the characteristics of linear polarization, and acquires the characteristics of "azimuthal polarization" at the radius corresponding to the critical scattering angle $\theta_{\rm f} = 1/\gamma$ and then returns to circular polarization if the radius continues to increase beyond the critical scattering angle.

5 Experiment

Recently, we conducted a test run of the spatial distribution measurement of LCSS gamma rays with a linearly polarized CO_2 laser at SLEGS. The electron beam current was 200 mA, and the CO_2 laser power was approximately 10 W. The incident CO_2 laser was approximately 100% linearly

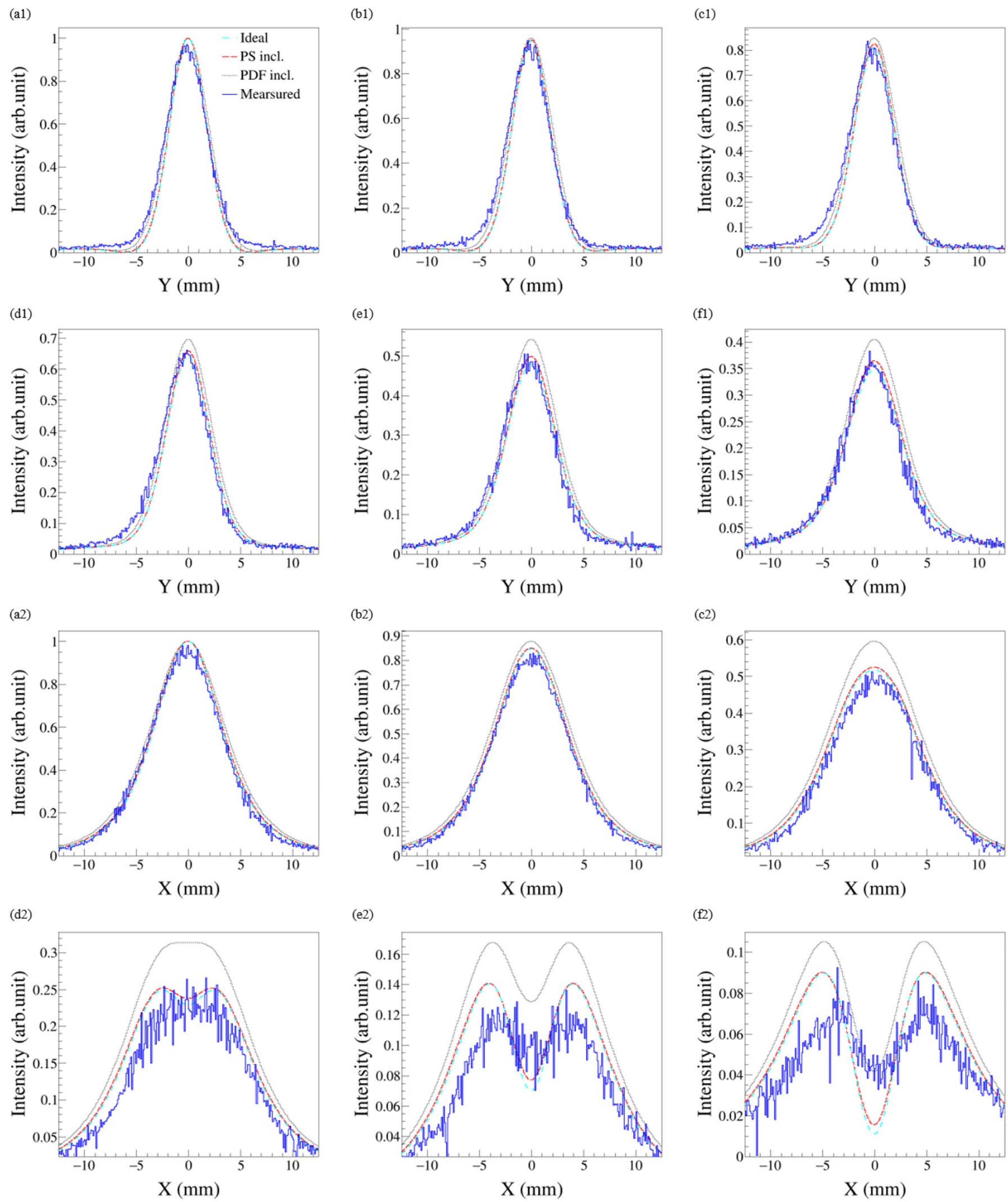

Fig. 10 (Color online) The intensity distribution of gamma spot along different slices: the fully ideal case ("Ideal", cyan line); the case incorporating electron position and momentum information ("PS incl.", red line); the case with point diffusion function included ("PDF incl.", black line); and experimentally measured 90° scattering imaging results ("Measured", blue line). Where **a1** is the result of the slice at the short axis, and **b1**, **c1**, **d1**, **e1**, and **f1** are the slices at distances of 1, 2, 3, 4, and 5 mm from **a1** along the *x*-axis, respectively. In contrast, **a2** is the result of slicing at the long axis, and **b2**, **c2**, **d2**, **e2**, and **f2** are slices at distances of 1, 2, 3, 4, and 5 mm from a2 along the *y*-axis, respectively

polarized. The aperture of the double collimator system was set to 20 and 40 mm for the upstream coarse collimator and downstream fine collimator, respectively, to ensure that the scattered gamma-ray beam was not blocked. The spatial distribution was measured at three slant incident angles of 60°, 90°, and 120° with the GSM [45]. The background gamma rays were measured by turning off the laser and subtracting them from the images recorded of the total radiation distribution.

Figure 8 shows the measured spatial distributions of the scattered gamma rays in the 2D and 3D frames. Comparing Figs. 8 and 6, the measured polarization shape and size of the scattered gamma spatial distribution are in general agreement with the simulations, which basically ensures the reliability of the simulation results. A tilt was observed between the measured direction of the gamma beam spot and the simulation results. This discrepancy was attributed to the rotation of the polarization angle in the initial laser optical path setup. The deviation remained consistent across all incident angles, and this stable offset supported this interpretation.

A further comparison between Figs. 8 and 6 shows that the size of the measured spatial distributions of scattered gamma rays is larger than that of the simulated ones for all three slant incident angles. The measured spot sizes are listed in Table 4. The fluorescence of the LYSO crystal in the GSM scattered inside the crystal is inferred to account for the enlargement of the gamma spot size. The introduced point spread function leads to the extra diffusion of the measured gamma spot. The point spread function (PSF) was measured using the knife-edge method, employing two perpendicularly placed lead bricks to block the gamma-ray spots. The results are shown in Fig. 9, with the PSF obtained through fitting. The obtained PSF was incorporated into the simulation program and compared with experimental results. As shown in Fig. 10, the cross-sectional comparisons of the gamma spot at different positions reveal that, while the intensity of the simulated profiles including the PSF is higher than the experimental values, their shape matches the experimental data more closely. In particular, for the cross-section at $Y = 5$ mm shown in subfigure (c4), the simulation result without the PSF drops to nearly zero at $X = 0$ mm. In contrast, both the simulation incorporating the PSF and the experimental results decreased to approximately half of their maximum values.

6 Summary and outlook

A simulation code was developed to study the characteristics of gamma beams produced by the novel laser Compton slant scattering mode at SLEGS. The intensity spatial distributions of the LCSS gamma-ray and the corresponding Stokes parameters were calculated by considering both linearly and circularly polarized incident laser cases. The simulation showed that for a linearly polarized laser, the direction of the scattered polarized gamma-ray spatial distribution changed with the slant of the incident angle. The present study also shows that the DOP of the incident photon is almost completely transferred to the scattered gamma rays for an arbitrary slant incident angle at the SLEGS.

A test run of the spatial distribution measurement using a linearly polarized CO_2 laser at SLEGS was conducted. The measured polarization direction and size of the scattered gamma spatial distribution were in good agreement with the simulations. Next, we investigated the direction and degree of polarization at various positions of the gamma-ray spot. Attempts will be made to extract the detailed efficiency of DOP transfer from laser to gamma-ray at different incident angles in the LCSS process using the GSM and other methods.

Acknowledgements We would like to thank the continued assistance from the Departments of Accelerator and Beamline Engineering at SSRF for their technical support.

Author Contributions All authors contributed to the study conception and design. Material preparation, data collection, and analysis were performed by Xiang-Fei Wang. The first draft of the manuscript was written by Xiang-Fei Wang and all authors commented on previous versions of the manuscript. All authors read and approved the final manuscript.

Data Availability The data that support the findings of this study are openly available in Science Data Bank at https://cstr.cn/31253.11.sciencedb.j00186.00991 and https://doi.org/10.57760/sciencedb.j00186.00991.

Declarations

Conflict of interest Hong-Wei Wang is an editorial board member for Nuclear Science and Techniques and was not involved in the editorial review, or the decision to publish this article. All authors declare that there are no conflict of interest.

References

1. H.R. Weller, M.W. Ahmed, H. Gao et al., Research opportunities at the upgraded HIγS facility. Prog. Part. Nucl. Phys. **62**, 257–303 (2009). https://doi.org/10.1016/j.ppnp.2008.07.001
2. A. Zilges, D. Balabanski, J. Isaak et al., Photonuclear reactions–From basic research to applications. Prog. Part. Nucl. Phys. **122**, 103903 (2022). https://doi.org/10.1016/j.ppnp.2021.103903
3. C. Schaerf, Polarized gamma-ray beams. Phys. Today **582**, 44 (2005). https://doi.org/10.1063/1.2062918
4. B. Neumcke, Production of circular polarized γ-rays by coherent bremsstrahlung of longitudinal polarized electrons. Phys. Lett. **23**, 382–384 (1966). https://doi.org/10.1016/0031-9163(66)90476-8
5. K.M. Watson, Some general relations between the photoproduction and scattering of pi mesons. Phys. Rev. **95**, 228 (1954). https://doi.org/10.1103/PhysRev.95.228
6. H. Überall, High-energy interference effect of bremsstrahlung and pair production in crystals. Phys. Rev. **103**, 1055 (1956). https://doi.org/10.1103/PhysRev.103.1055
7. G. Bologna, G. Diambrini, G.P. Murtas, High-energy bremsstrahlung from a silicon single crystal. Phys. Rev. Lett. **4**, 572 (1960). https://doi.org/10.1103/PhysRevLett.4.572
8. L. Casano, A. Marino, G. Matone et al., Production of a beam of polarized and monochromatic gamma rays by Compton scattering

of laser light against high-energy electrons. Report No. LNF74/60, LNF or Laboratori Nazionali di Frascati, 1974. https://inspirehep.net/literature/91360
9. G. Kezerashvili, A. Milov, N. Muchnoi et al., A Compton source of high energy polarized tagged gamma-ray beams the ROKK-1M facility. Nucl. Instrum. Methods Phys. Res., Sect. B **145**, 40 (1998). https://doi.org/10.1016/S0168-583X(98)00266-3
10. J. Bocquet, J. Ajaka, M. Anghinolfi et al., GRAAL: a polarized γ-ray beam at ESRF. Nucl. Phys. A **622**, c124–c129 (1997). https://doi.org/10.1016/S0375-9474(97)00337-0
11. A. Sandorfi, M. LeVine, C. Thorn et al., High energy gamma ray beams from Compton backscattered laser light. IEEE Trans. Nucl. Sci. **30**, 3083–3087 (1983). https://doi.org/10.1109/TNS.1983.4336577
12. J. Yan, J.M. Mueller, M.W. Ahmed et al., Precision control of gamma-ray polarization using a crossed helical undulator free-electron laser. Nat. Photonics **13**, 629–635 (2019). https://doi.org/10.1038/s41566-019-0467-6
13. T. Nakano, J. Ahn, M. Fujiwara et al., Multi-GeV laser-electron photon project at SPring-8. Nucl. Phys. A **684**, 71–79 (2001) https://doi.org/10.1016/S0375-9474(01)00490-0
14. N. Muramatsu, M. Yosoi, T. Yorita et al., SPring-8 LEPS2 beamline: a facility to produce a multi-GeV photon beam via laser Compton scattering. Nucl. Instrum. Methods Phys. Res. Sect. A-Accel. Spectrom. Dect. Assoc. Equip. **1033**, 166677 (2022). https://doi.org/10.1016/j.nima.2022.166677
15. R.W. Schoenlein, P. Leemansa, H. Chin et al., Femtosecond X-ray pulses at 0.4 Å generated by 90° Thomson scattering: a tool for probing the structural dynamics of materials. Science **274**, 236 (1996). https://doi.org/10.1126/science.274.5285.236
16. H. Ohgaki, S. Koda, Y. Iwasaki et al., Study on energy variable laser-compton gamma-ray with a fixed energy electron beam. J. Nucl. Sci. Technol. **44**, 698–702 (2007). https://doi.org/10.3327/jnst.44.698
17. Y. Taira, S. Endo, S. Kawamura et al., Measurement of the spatial polarization distribution of circularly polarized gamma rays produced by inverse Compton scattering. Phys. Rev. A **107**, 063503 (2023). https://doi.org/10.1103/PhysRevA.107.063503
18. Y. Taira, Spatial distribution of gamma rays produced by axially symmetric polarized and optical vortex lasers. Phys. Rev. A **110**, 043525 (2024). https://doi.org/10.1103/PhysRevA.110.043525
19. Y. Taira, Y. Yang, T. Shizuma et al., Generation and measurement of gamma rays with axially symmetric polarization states via Compton scattering. Phys. Rev. Res. **7**, 033130 (2025). https://doi.org/10.1103/pn68-rjd2
20. C. Sun, Y.K. Wu, Theoretical and simulation studies of characteristics of a Compton light source. Phys. Rev. ST Accel. Beams **14**, 044701 (2011). https://doi.org/10.1103/PhysRevSTAB.14.044701
21. V. Petrillo, A. Bacci, C. Curatolo et al., Polarization of X-gamma radiation produced by a Thomson and Compton inverse scattering. Phys. Rev. ST Accel. Beams **18**, 110701 (2015). https://doi.org/10.1103/PhysRevSTAB.18.110701
22. Z. Chi, Polarization transfer from a laser to X-rays via Thomson scattering with relativistic electrons: a dipole radiation perspective. J. Appl. Phys. **128**, 244904 (2020). https://doi.org/10.1063/5.0029390
23. Z. Chi, X-ray polarization characteristics in the nonlinear Thomson scattering of a laser with relativistic electrons. Nucl. Instrum. Methods Phys. Res. Sect. A **1033**, 166681 (2022). https://doi.org/10.1016/j.nima.2022.166681
24. Z. Chi, H. Zhang, J. Lin et al., A Monte Carlo simulation method for polarized gamma-ray nuclear resonance fluorescence. Nucl. Instrum. Methods Phys. Res. Sect. A **1056**, 168666 (2023). https://doi.org/10.1016/j.nima.2023.168666
25. Z. Chi, L. Yan, Y. Du et al., Recent progress of phase-contrast imaging at Tsinghua Thomson-scattering X-ray source. Nucl. Instrum. Methods Phys. Res. Sect. B **402**, 364–369 (2017).https://doi.org/10.1016/j.nimb.2017.02.062
26. Z. Chi, Y. Du, W. Huang et al., Linearly polarized X-ray fluorescence computed tomography based on a Thomson scattering light source: a Monte Carlo study. J. Synchrot. Radiat. **27**, 737–745 (2020). https://doi.org/10.1107/S1600577520003574
27. H. Zhang, Y. Du, Z. Chi et al., Experimental demonstration of polarization control in Thomson scattering X-ray sources. Nucl. Instrum. Methods Phys. Res. Sect. A **1064**, 169376 (2024). https://doi.org/10.1016/j.nima.2024.169376
28. M. Jiang, X. Yang, H. Xu et al., Shanghai synchrotron radiation facility. Chin. Sci. Bull. **54**, 4171–4181 (2009). https://doi.org/10.1007/s11434-009-0689-y
29. X. Wu, S. Tian, X. Liu et al., Design and commissioning of the new SSRF storage ring lattice with asymmetric optics. Nucl. Instrum. Methods Phys. Res. Sect. A **1025**, 166098 (2022). https://doi.org/10.1016/j.nima.2021.166098
30. H. Xu, G. Fan, H. Wang et al., Interaction chamber for laser Compton slant-scattering in SLEGS beamline at Shanghai Light Source. Nucl. Instrum. Methods Phys. Res. Sect. A **1033**, 166742 (2022). https://doi.org/10.1016/j.nima.2022.166742
31. Z. Hao, G. Fan, H. Wang et al., The day-one experiment at SLEGS: systematic measurement of the (γ, 1n) cross sections on ^{197}Au and ^{159}Tb for resolving existing data discrepancies. Sci. Bull. **70**, 2591–2597 (2025). https://doi.org/10.1016/j.scib.2025.05.037
32. H. Xu, H. Utsunomiya, G. Fan et al., Gamma-ray flux in Gated CW operation of CO_2 laser at SLEGS. Nucl. Instrum. Methods Phys. Res. Sect. A **1073**, 170249 (2025). https://doi.org/10.1016/j.nima.2025.170249
33. L. Liu, H. Utsunomiya, G. Fan et al., Energy profile of laser Compton slant-scattering γ-ray beams determined by direct unfolding of total-energy responses of a BGO detector. Nucl. Instrum. Methods Phys. Res. Sect. A **1063**, 169314 (2024). https://doi.org/10.1016/j.nima.2024.169314
34. Z. Hao, G. Fan, H. Xu et al., Quasi-monochromatic gamma beam modulation at SLEGS. Radiat. Meas. **174**, 107127 (2024). https://doi.org/10.1016/j.radmeas.2024.107127
35. Z. Hao, G. Fan, H. Wang et al., Collimator system of SLEGS beamline at Shanghai Light Source. Nucl. Instrum. Methods Phys. Res. Sect. A **1013**, 165638 (2021). https://doi.org/10.1016/j.nima.2021.165638
36. Z. Hao, G. Fan, H. Wang et al., A new annular collimator system of SLEGS beamline at Shanghai Light Source. Nucl. Instrum. Methods Phys. Res. Sect. B **519**, 9–14 (2022). https://doi.org/10.1016/j.nimb.2022.02.010
37. H. Wang, G. Fang, W.-Q. Shen et al., SLEGS: the first photonuclear reaction research platform in China. Nucl. Phys. News **33**, 17–22 (2023). https://doi.org/10.1080/10619127.2023.2230858
38. L. Liu, H. Wang, G. Fan et al., The SLEGS beamline of SSRF. Nucl. Sci. Tech. **35**, 111 (2024). https://doi.org/10.1007/s41365-024-01469-3
39. L. Landau, E. Lifshitz, The classical theory of fields. (Butterworth-Heinemann, 1975)
40. S. Park, V. Litvinenko, W. Tornow et al., Spatial distribution and polarization of γ-rays generated via Compton backscattering in the Duke/OK-4 storage ring FEL. Nucl. Instrum. Methods Phys. Res. Sect. A**475**, 425–431 (2001). https://doi.org/10.1016/S0168-9002(01)01635-7
41. R. Tai, Z. Zhao, Commissioning and first results of the SSRF phase-II be amline project. J. Phys: Conf. Ser. **2380**, 012004 (2022). https://doi.org/10.1088/1742-6596/2380/1/012004
42. R. Tai, Z. Zhao, Overview of SSRF phase-II beamlines. Nucl. Sci. Tech. **35**, 137 (2024). https://doi.org/10.1007/s41365-024-01487-1

43. H. Wang, G. Fan, L. Liu et al., Commissioning of laser electron gamma beamline SLEGS at SSRF. Nucl. Sci. Tech. **33**, 87 (2022). https://doi.org/10.1007/s41365-022-01076-0
44. H. Xu, G. Fan, Laser transport system of shanghai laser electron gamma source (SLEGS). in *12th International Particle Accelerator Conference (IPAC'21), Campinas, SP, Brazil, 24–28 May 2021, JACOW Publishing, Geneva, Switzerland, 2021*, pp. 3897–3900 (2021). https://doi.org/10.18429/JACoW-IPAC2021-THPAB063
45. Z. Hao, H. Xu, G. Fan et al., Gamma Spot Monitor at SLEGS beamline. Nucl. Instrum. Methods Phys. Res. Sect. A**1068**, 169748 (2024). https://doi.org/10.1016/j.nima.2024.169748
46. D. Filipescu, Monte Carlo simulation method of polarization effects in Laser Compton Scattering on relativistic electrons. J. Instrum. **17** P11006 (2022). https://doi.org/10.1088/1748-0221/17/11/P11006